Composites Part B 264 (2023) 110924

Contents lists available at ScienceDirect

Composites Part B

journal homepage: www.elsevier.com/locate/compositesb

Investigation of welding repair methods for thermoplastic composite joints

Wencai Li, Genevieve Palardy *

Department of Mechanical and Industrial Engineering, Louisiana State University, 3261 Patrick F. Taylor Hall, Baton Rouge, LA, 70803, United States

ARTICLE INFO

Handling Editor: Dr Uday Vaidya

Keywords:
Thermoplastic composites
Nanocomposite films
Repair
Ultrasonic welding
Resistance heating

ABSTRACT

Repair is a common process to extend the service life of composite structures, and there is a need for techniques compatible with thermoplastic composites (TPCs). As the assembly of TPC joints through welding is gaining importance, evaluating their potential for repairability is essential. This work aims to develop novel techniques to repair welded TPC joints: 1) Successive repair (three cycles) of broken joints by ultrasonic-assisted method with neat and nanocomposite films, and 2) one-step repair using ultrasonic welding (USW) and resistance heating. It was found from tensile testing that multi-walled carbon nanotube/polypropylene (MWCNT/PP) films partially restored the lap shear strength (LSS), but pure PP films enabled significant recovery of the LSS as 94.5%, 89.4%, and 86.7% after the first, second, and third repair cycle, respectively. Nanocomposite films were however promising for monitoring the initiation and propagation of the damage occurring within the repaired joints, even after three repair cycles. Moreover, results from one-step repair using USW revealed that a stronger and more uniform repair interface was obtained, compared to resistance heating. Overall, the repair methods developed in this study exhibited promise for TPC joint repair, with strength recovery between 63.8% and 94.5%.

1. Introduction

Thermoplastic composites (TPCs) are increasingly used in aerospace, automotive, maritime, energy, biomedical, oil & gas, and sporting goods, where strength, weight, and sustainability are of vital importance. These applications have created a demand for large or integrated structural components. However, composite structures sustain consistent load and environmental damage during their service life, which threatens their structural integrity [1], leading to an increasing interest in composite repair techniques. To address damage, the capability to repair structures and recovery of their mechanical properties are important considerations and much attention has been paid to developing effective repair methods [2].

The most common repair techniques for composite structures, predominantly applied to thermoset composites, include resin injection/infusion, mechanically fastened repair, and bonded repair. Injecting liquid resin into delamination or damaged regions may however lead to contamination from the environment [3]. While mechanical fastening is a reliable repair method and has been widely used in industry, it can introduce stress concentration through fastener holes and increase the weight of composite structures. Furthermore, mechanical fasteners are susceptible to galvanic corrosion [4]. On the other hand, bonded repair (scarf repair and patch repair), another repair method commonly used in industry, alleviates some of those disadvantages and may easily be formed [1,2,5–8]. The effect of the stacking sequence of parent laminates, as well as the stacking sequence of external patches, on the repair behavior under fatigue loading [8] and tensile loading [1] was investigated by the same research group. Additionally, the adhesive plays an important role in the efficiency and durability of patch repairs. For instance, Ji et al. [6] proposed a bi-adhesive repair construction with carbon nanotubes (CNTs) incorporation into epoxy resin adhesive for glass fiber (GF)/epoxy patch repair. They concluded that 0.5 wt% CNTs increased the ultimate failure load and bi-adhesive repair provided a better repair quality, higher maximum displacement to failure, lower stress concentration at the damaged region, and superior fracture toughness than repairing with single adhesive alone. Nevertheless, patch repair typically presents an uneven surface at the repair site and thus affects the distribution of internal loadings in the materials. On the other hand, the removal of damaged areas and replacement with the pristine materials make scarf repair potentially complicated to implement. To address these issues, Li et al. [9] incorporated thermoplastic particles into thermosetting adhesive for self-healing of damaged adhesively bonded double cantilever beam composite joints. Then, thermoplastic mendable filaments, used as healing agents, were integrated into a carbon fabric to repair delamination damage in CF/epoxy [10] and z-pinned CF/epoxy composites [11]. Adhesive bonding can however be

* Corresponding author.
E-mail address: gpalardy@lsu.edu (G. Palardy).

https://doi.org/10.1016/j.compositesb.2023.110924
Received 22 May 2023; Received in revised form 13 July 2023; Accepted 29 July 2023
Available online 30 July 2023

challenging for TPCs because the thermoplastic matrix possesses low surface free energy, making it difficult to wet the surface and create a strong bond.

Since thermoplastics soften when heated above their glass transition temperature (T_g) for amorphous polymers or melting temperature (T_m) for semi-crystalline polymers, fusion bonding (welding) may be leveraged for repair [4]. In particular, ultrasonic welding (USW), a promising welding technique due to its short processing time and low energy consumption, applies pressure with a sonotrode and then ultrasonic vibration at the interface to be welded. An energy director (ED), or thermoplastic film, is typically used to promote heat generation at the interface through surface friction and viscoelastic heating [12–18], but spot welding without ED has also been successfully demonstrated [19–22]. Previous work investigated the use of CNT/thermoplastic films to enable multifunctionality for ultrasonically welded TPC joints: i) energy direction during the USW process [23]; ii) damage sensing for structural health monitoring through electrical resistance measurements under various mechanical loading types [23–25]; and iii) resistance heating-assisted disassembly of welded joints [26], then repair [27]. All those functions have been studied in depth in previous work, except the repair capabilities with resistance or ultrasonic welding, which is still limited in the literature for TPCs and their joints.

Resistance welding is a convenient welding method because it requires little to no surface preparation, simple tooling, and low cost of equipment [28]. It uses an electrically resistive film called heating element sandwiched between two parts. When an electric current passes through the element, temperature rises by Joule heating. Once the temperature of the bond line increases to a certain point (T_g for amorphous or T_m for semi-crystalline polymers), the thermoplastic matrix will start to melt and diffuse at the interface. When a predefined temperature is reached, the material cools down and solidifies under sufficient pressure. In literature and industry, three main types of heating elements are frequently used. Carbon fiber was popular in the early stages of research due to its compatibility with composite laminates. CF/polypropylene (PP) was proposed by Hou and Friedrich as a heating element to join CF/PP [29] and GF/PP composites [30]. In a later work, Ageorges et al. [28,31] welded CF and GF reinforced polyetherimide (PEI) laminates by using unidirectional and fabric CF/PEI heating elements, respectively. They concluded that fabric heating elements presented a more uniform temperature distribution, higher lap shear strength (LSS), and higher interlaminar fracture toughness than using unidirectional heating elements. Subsequently, stainless steel mesh was found to deliver better consistency, as well as higher strength compared to CF heating elements [32]. In Ref. [33], stainless steel mesh heating elements were introduced into a skin/stringer joint configuration to weld APC-2/AS4 PEEK composites. Fractographic analysis of the fracture surfaces carried out by Barbosa et al. [34] showed good bonding between the heating element mesh and the polymer matrix at the welding region. More recently, a new type of heating element consisting of electrically conductive nanoparticles (multi-walled carbon nanotubes, MWCNTs) was developed [35]. This novel element was completely miscible within the polymer matrix and its coefficient of thermal expansion was better matched to the adherends than the steel mesh. Therefore, the thermal residual stress was reduced when using nanocomposite-based heating elements [36].

Although welding of TPCs has been widely studied over the past few years, mostly as a joining technique, it is expected that the welded joints can be repaired by re-welding the broken components or using assistive heating methods for localized repair. Therefore, this work presents novel repair concepts involving 1) ultrasonic welding with successive use of nanocomposite films to enable cyclic repair while simultaneously maintaining their damage monitoring capability, and 2) direct repair of fractured joints under resistance heating and ultrasonic welding. The main goal of this study is to assess the feasibility of the proposed repair techniques and their strength recovery. Hence, the behavior of repaired GF/PP joints under tensile loading after each repair cycle was investigated. The failure modes of the repaired joints were observed by optical and scanning electron microscopy, to provide insight on the effect of repair cycles on strength recovery. The repair capacity of ultrasonic welding and resistance heating methods was compared through mechanical testing and fractography analysis. Finally, electrical resistance measurements were used to analyze the damage sensing capability of nanocomposite films in the cyclically repaired joints. The outcomes of this work contribute new knowledge into the effectiveness of fusion bonding repair techniques for TPC joints.

2. Materials and experimental methods

2.1. Materials and sample preparation

Pure PP films were manufactured from PP pellets, with a granule size of 5 mm and a melt flow rate (MFR) of 6 g/min, supplied by Goodfellow (Coraopolis, PA, USA). Nanocomposite films were prepared from 15 wt % multi-walled carbon nanotube/polypropylene (MWCNT/PP) pellets purchased from Cheap Tubes Inc. (Grafton, VT, USA). These pellets were produced by twin-screw extrusion. This weight fraction was selected based on previous research [24]. The laminates were made from eight layers of 0.33 mm-thick unidirectional (UD) glass fiber/polypropylene (GF/PP) prepregs (IE 6030) provided by Avient (formerly PolyOne, Avon Lake, OH, USA), stacked in a $[0]_8$ sequence with a 60% fiber volume fraction. The melting point of the PP matrix was determined by differential scanning calorimetry (DSC) as about 164.6 °C. The incorporation of MWCNTs and GF slightly affected the melting temperature (162.8 °C for 15 wt% MWCNT/PP and 162.9 °C for GF/PP). PP and MWCNT/PP films (with 0.5 mm thickness), as well as GF/PP laminates were fabricated following procedures [24] schematically illustrated in Fig. 1.

2.2. Ultrasonic welding and repair

A Dynamic 3000 ultrasonic welder (Rinco Ultrasonics, Danbury, CT, USA) with a 20 kHz frequency and a maximum power of 3000 W was used to join single lap shear specimens with an overlap of 12.7 mm in length (L) and 25.4 mm in width (W). The vibration amplitude was obtained through a booster gain of 1:1.5 and a sonotrode gain (diameter of 40 mm) of 1:3.85. Prior to welding, the surfaces of the adherends and nanocomposite film were cleaned with ethyl alcohol. Two adherends and a pure PP or nanocomposite film (called “energy director” (ED)) were installed on the welding fixture with a pair of customized clamps (Fig. 2a), allowing vertical movement of the upper adherend. The film (ED) was used to locally increase temperature at the interface under ultrasonic vibration and create a strong single lap joint over the 12.7 mm × 25.4 mm area [12–14,37]. A constant welding force of 1000 N

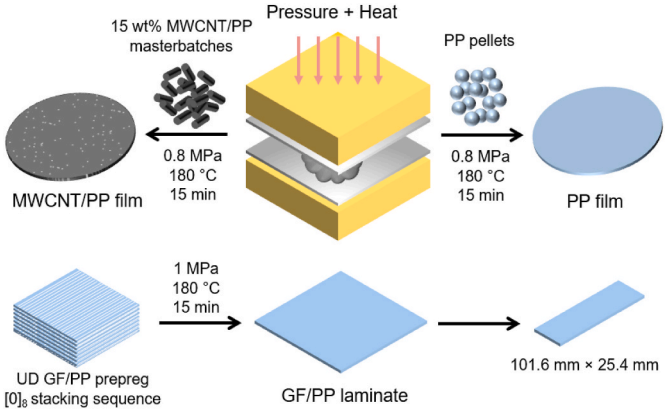

Fig. 1. Schematic of preparation for PP films, MWCNT/PP films, and GF/PP laminates via compression molding.

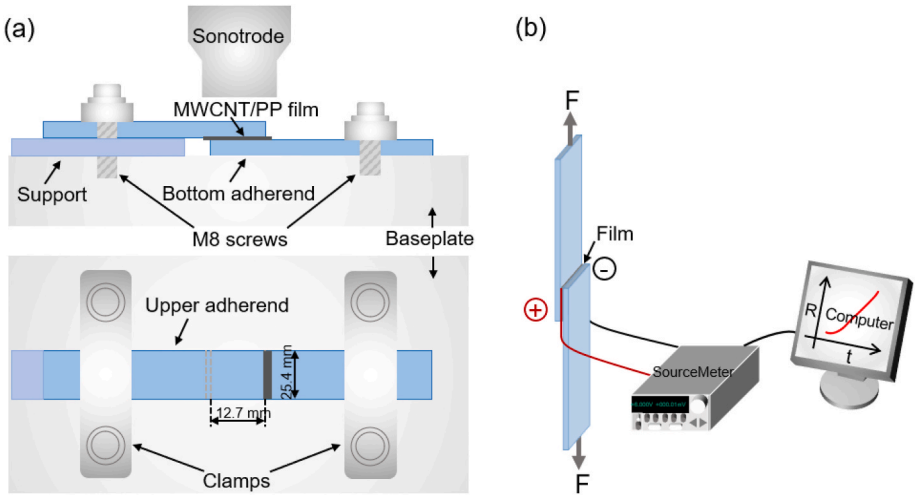

Fig. 2. Schematic of (a) USW and (b) single-lap tensile testing and electrical resistance measurement setup.

with a 38.1 μm vibration amplitude was applied, followed by a solidification step under the same force for 4000 ms. The ultrasonic welder was set to stop the downward movement of the sonotrode when its vertical displacement reached a pre-determined "travel" value. The single lap joints (SLJs) in this work will be referred to as "PP-GF/PP" and "MWCNT/PP-GF/PP" SLJs.

After tensile fracture on a universal testing machine (detailed in Section 2.4), the SLJs were repaired via USW according to the aforementioned procedure, with and without energy directing films. The edges of the specimen were trimmed prior to repair to remove the irregularities obtained from the joining process due to the transverse flow of film that might affect the repair. A new PP film or MWCNT/PP film was placed between the fractured joints to enable ultrasonic-assisted repair. The vertical displacement of the sonotrode was controlled by a travel value of 60% (i.e., 60% of the initial film thickness). In this way, three repair and tensile fracture cycles were performed to establish the repair effectiveness of successive operations. To assess effectiveness of repair without films, joints were also directly repaired, without insertion of a new film at the interface. This repair process was compared for different travel values as they were expected to influence fiber/polymer deformation and squeeze out at the weld line, thus with 20%, 40%, and 60% travel based on film thickness.

2.3. Resistance heating repair

The experimental setup used for resistance heating (RH) repair is shown in Fig. 3a. After tensile testing (detailed in Section 2.4), the broken MWCNT/PP film was leveraged to act as a heating element. First, both adherends were positioned back into a single lap configuration. To establish electrical connection, silver paint (SPI #05002-AB) was then applied along the edges of the overlap. Two standard 30 AWG copper wires were placed on both sides of the weld interface, running along its length, and fixed with polyimide tape. The joint to be repaired was sandwiched between two ceramic blocks as insulators to reduce heat losses and facilitate uniform pressure distribution on the heating surface. During the repair process, a constant voltage was supplied by a Keithley 2604B SourceMeter with a maximum current output of 10 A and maximum voltage output of 40 V. A spring clamp was used to apply a pressure of approximately 0.2 MPa, which falls within the range of reported optimal pressures, 0.15–0.4 MPa, for TPCs [38]. It was shown that a suitable pressure is able to ensure intimate contact between heating element and adherends, allowing good mechanical properties, and promote molecular diffusion at the interface, while removing voids because of polymer flow squeezed out of the heating zone [36]. Temperature measurements throughout the RH process were carried out using a type-K thermocouple connected to a TC-08 Data Logger (Pico Technology, Tyler TX, USA). The thermocouple was located at the center of the joint (1/2 W and 1/2 L) and above the repair zone, between top adherend and ceramic block (Fig. 3b), where the measured temperature was confirmed to be close to the temperature within the joints ($\Delta T < 3\ ^{\circ}C$). The thermocouple was not embedded directly at the interface because the fracture surface was uneven after the initial welding, which might affect current flow and thus weaken the intimate contact. The data was acquired at a rate of 100 points per millisecond by PicoLog 6 software. When the temperature reached a pre-determined heating point, the voltage was stopped from being supplied.

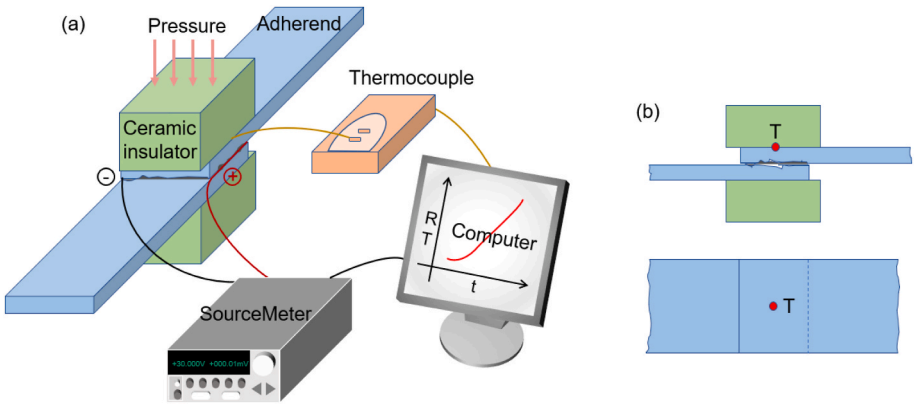

Fig. 3. Schematic illustration of (a) RH repair setup and (b) location of the thermocouple during RH process.

2.4. Mechanical tests and morphological characterization

Tensile testing was carried out to assess the mechanical properties of reference and repaired joints based on the ASTM D1002 standard. The setup is shown in Fig. 2b. After each repair cycle, testing was performed using a 50 kN universal testing machine (Model 313, TestResources) with a crosshead speed of 1.3 mm/min until fracture of the joint. Two square grips were offset to ensure initial parallelism between load and weld lines. The free length of SLJ between the two grips was 60 mm. The lap shear strength (LSS) was calculated as the maximum load divided by the joint area. Similarly, the joints repaired by USW and RH without inserting a new film at the interface were tested to determine the strength recovery according to the same process. Five specimens were tested for each repair case to obtain the average LSS and standard deviation. In order to remove the outliers, Chauvenet's Criterion method was used when analyzing the data.

After fracture, naked-eye observation was first used to examine the effect of cyclic repair operations on the failure modes for ultrasonically repaired SLJs with ED, and the influence of travel values on the failure mechanisms of repaired joints without ED. An optical microscope (Meiji MT8100) was employed for cross-sectional analysis of USW and RH repaired joints. The cross-section was embedded into an epoxy resin mold, ground with 180, 360, 600, 800, and 1200 grit SiC pressure sensitive adhesive (PSA)-backed abrasive papers, and then polished with 6 and 1 μm diamond solutions, respectively, followed by a rinse with distilled water and ethanol. To better understand failure mechanisms after repair, the fracture surfaces of all repaired joints were further observed using a focused ion beam (FIB) high-resolution field emission gun scanning electron microscope (FEI QUANTA 3D FEG FIB/SEM). Before observation, a sputter coater (EMS550X) was used to coat fracture surfaces with gold under a vacuum of 1×10^{-1} mbar and 25 mA for 4 min to increase their conductivity.

2.5. Damage monitoring of cyclically repaired joints

Nanocomposite-based monitoring involves capturing the electrical resistance changes of polymer matrix specimens under mechanical strain, enabled by electrically conductive nanoparticles. For repaired joints, the resistance profiles obtained from nanocomposite-based monitoring at the welded interface enable damage detection within the repaired regions and evaluate sensing capability of nanocomposite films. The Keithley KickStart software was used to capture resistance changes. A voltage of 6 V was supplied to the repaired joint by a Keithley SourceMeter 2604B. The preparation of the specimens for damage monitoring involved sealing copper wires to the weld line (Fig. 2b) using silver paint (SPI #05002-AB) to reduce the contact resistance and minimize the effect of wire position with respect to the thin weld line. A cooling fan during the testing was placed close to the repaired joints to prevent the increase in temperature caused by Joule heating and thus avoid the influence of temperature on resistance measurements. Before applying loading, the electrical resistance of repaired joints was measured for 1 min to obtain the initial resistance (R_0). Since R_0 values exhibit significant deviation due to the experimental preparation variations and the measured electrical resistance may vary from one specimen to another, the change of electrical resistance ($\Delta R/R_0$ (%)) was used as a comparison method. At least five specimens were tested to ensure the repeatability of the experiments.

3. Results and discussion

3.1. USW cyclic repair with energy directors

3.1.1. Tensile behavior and failure mechanisms

Following the initial tensile testing, fully broken SLJs were repaired using the technique described in Section 2.2 with a new PP or MWCNT/PP film sandwiched between adherends. After repair, tensile testing was performed according to the previous process. Three successive repair cycles were carried out to assess whether ultrasonic-assisted repair was effective in re-bonding the fractured adherends and recovering their mechanical strength. Fig. 4a and b plot the typical load-displacement curves of cyclically repaired joints with USW, including the initial joint performance. It is observed that both PP-GF/PP and MWCNT/PP-GF/PP SLJs depict a very similar behavior. Failure load and corresponding displacement values decrease with the increasing number of repair cycles, as indicated by each dashed circle. Moreover, the ultimate load and elongation at break for the repaired joints are higher for PP-GF/PP SLJs when compared to MWCNT/PP-GF/PP SLJs.

Fractographic analysis was used to assess the morphology of repaired joints. Fig. 4c and d show representative fracture surfaces for both cases after the third repair cycle. It is noted that the fracture patterns in the polymer matrix are inconsistent. At the same scale and magnification, the matrix in PP-GF/PP SLJs is more intact and smoother than in MWCNT/PP-GF/PP joints, which confirms that PP films are more ductile and thus extend more under tension in Fig. 4a. The incorporation of MWCNTs creates a stiffer and more brittle nanocomposite polymer [39,40].

The results of single lap shear tests are illustrated in Fig. 5a. For repair with a PP film, 94.5%, 89.4%, and 86.7% of LSS with respect to the initial joint was recovered after the first, second, and third repair cycle, respectively. MWCNT/PP films partially restored the strength to a lesser extent (81.3%, 73.6%, and 63.8%). A few interrelated factors play a role in the re-bonding effectiveness of MWCNT/PP films, compared to specimens repaired with pure PP films. First of all, as the repair operation was repeated, the fracture surfaces of joints with MWCNT/PP films became more uneven due to their brittleness, compared to PP films, potentially resulting in a non-uniform temperature distribution at the weld interface and thus the degree of film melting was different. Secondly, as seen in inset in Fig. 5a, joints repaired with new MWCNT/PP films have a higher thickness increase at the weld line after three repair cycles than PP films, which may be another factor affecting strength recovery. In addition, as was previously observed in Ref. [23], lower performance of nanocomposite films might be caused by their brittleness compared to PP films. Finally, more significant fiber deformation (Fig. 5c (iii) and (iv)) occurs at the edges of the weld interface as films melt due to the increased viscosity with the incorporation of MWCNTs, which may accelerate the failure of MWCNT/PP film repaired joints, compared to PP-GF/PP SLJs, and further contribute to their reduction in LSS.

On the other hand, for both repair types, the average LSS gradually decreases as the number of repair cycles increases. This phenomenon can be explained by the macro/micro-structural observations at the weld interface. Visual inspection of the fracture surfaces after three repair cycles, including the initial joining, shows more unmolten films (Fig. 5b (iii) and Fig. 5c (iv)) and broken fibers (Fig. 5b (iv)) with the number of repair cycles for PP and MWCNT/PP film joints, likely responsible for reducing LSS. When fibers break, there is a lower contact area between fibers and matrix, and the interfacial shear stresses are concentrated at the ends of the fibers. As a result, the load-transfer capacity between the fibers and matrix is reduced, which will lead to a lower overall strength of the composite. In addition, when fibers break, the load they were bearing is transferred to the surrounding fibers, causing them to experience high stresses and potentially fail, contributing to the lower strength [41,42]. In addition, while interlaminar failure occurs in both adherends and propagates into the film for each repair cycle, it is worth noting that interfacial failure (between unmolten ED and GF/PP adherends) becomes progressively more apparent after the second and third repair cycles, which typically lowers joint strength. In Fig. 5d (ii), after the third repair cycle for MWCNT/PP-GF/PP SLJs, the number of broken fibers increases from the previous cycles, as observed in Fig. 5d (i), corresponding to the reduced LSS from the initial case to the third repair cycle. Considered together, the morphological changes of the repair interface, including unmolten film, broken fibers,

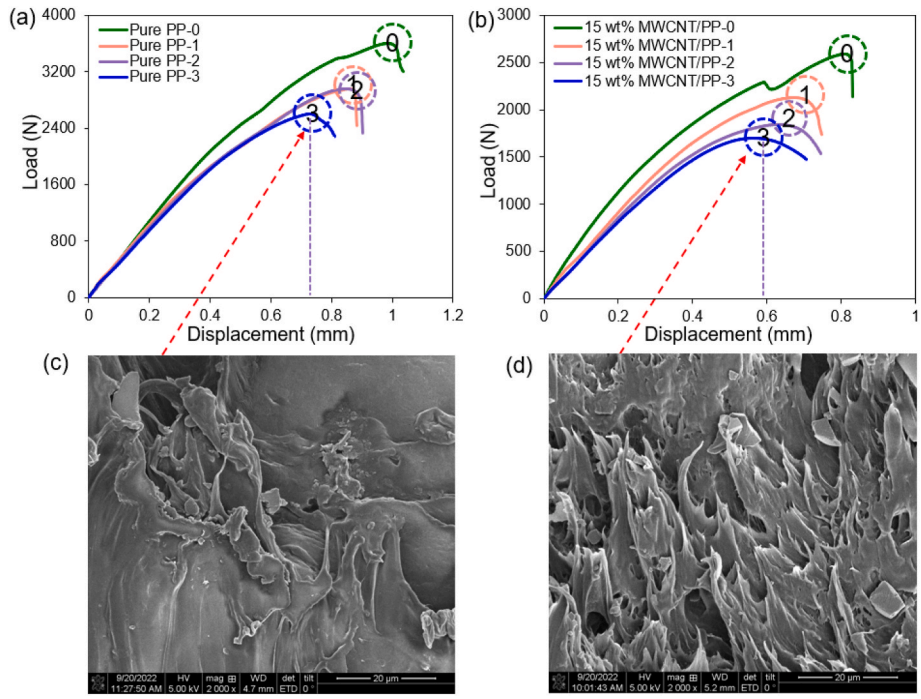

Fig. 4. Representative load-displacement curves for repaired specimens after each repair cycle: (a) PP-GF/PP and (b) MWCNT/PP-GF/PP SLJs (0, 1, 2, and 3 indicate the number of repair cycles and dashed circles indicate the position of peaks in load curves); SEM images of fracture surfaces after the third repair cycle for (c) PP-GF/PP and (d) MWCNT/PP-GF/PP SLJs.

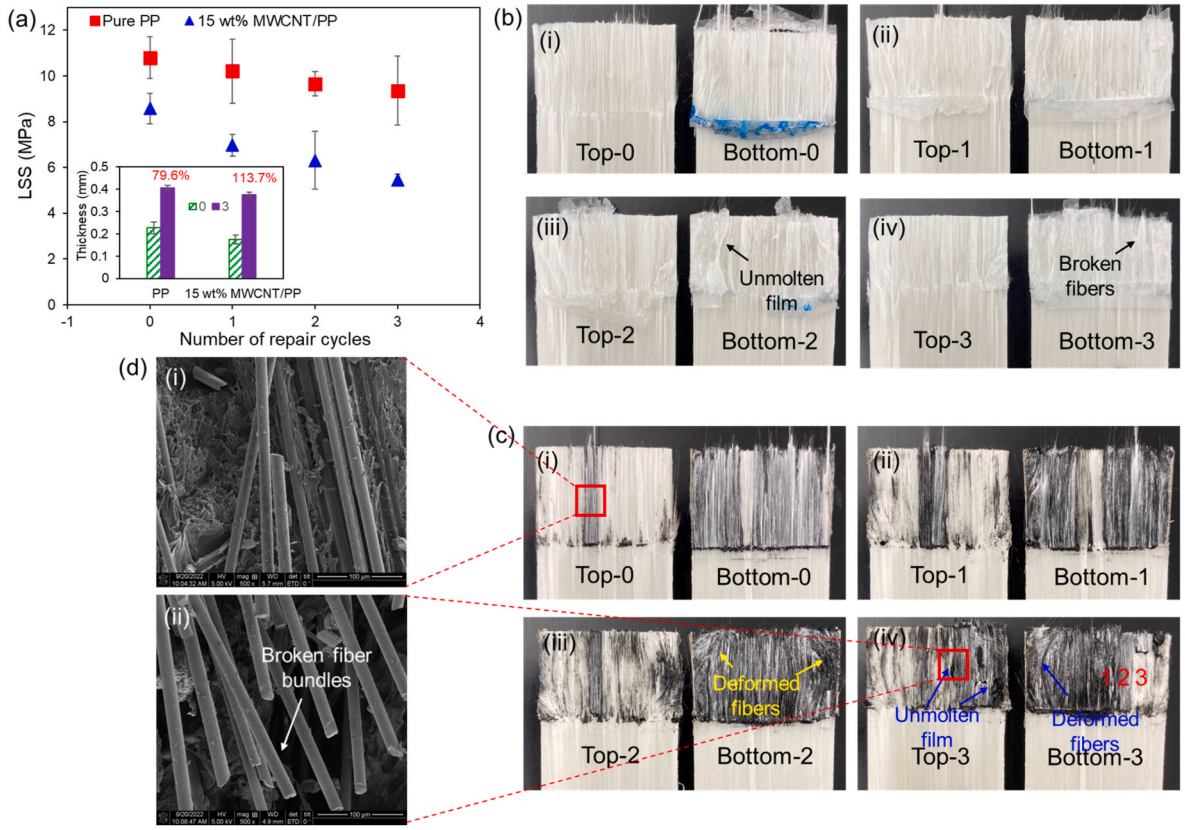

Fig. 5. (a) LSS of repaired GF/PP joints after each repair cycle (thickness of weld line before repair and after the third repair cycle in inset); (b) and (c) Fracture surfaces of PP-GF/PP and MWCNT/PP-GF/PP SLJs after each repair cycle: (i) initial, (ii) first, (iii) second, and (iv) third, respectively; and (d) SEM images of fracture surfaces of MWCNT/PP-GF/PP SLJs: (i) initial and (ii) third repair cycle.

deformed fibers, and different failure modes, explain the reduced mechanical properties as the number of repair cycles increases.

3.1.2. Damage monitoring capability after cyclic repair

To confirm the damage monitoring capability of nanocomposite films within repaired joints, the electrical resistance changes of cyclically repaired MWCNT/PP-GF/PP SLJs were further investigated. Fig. 6a–d show the load and percentage change of electrical resistance profiles for each repair cycle. It is worth noting that the electrical resistance of repaired SLJs, after the first cycle (Fig. 6b), still displays typical response characteristics analogous with the initial SLJs (Fig. 6a). At around 32 s, a slight increase in resistance is caused by damage

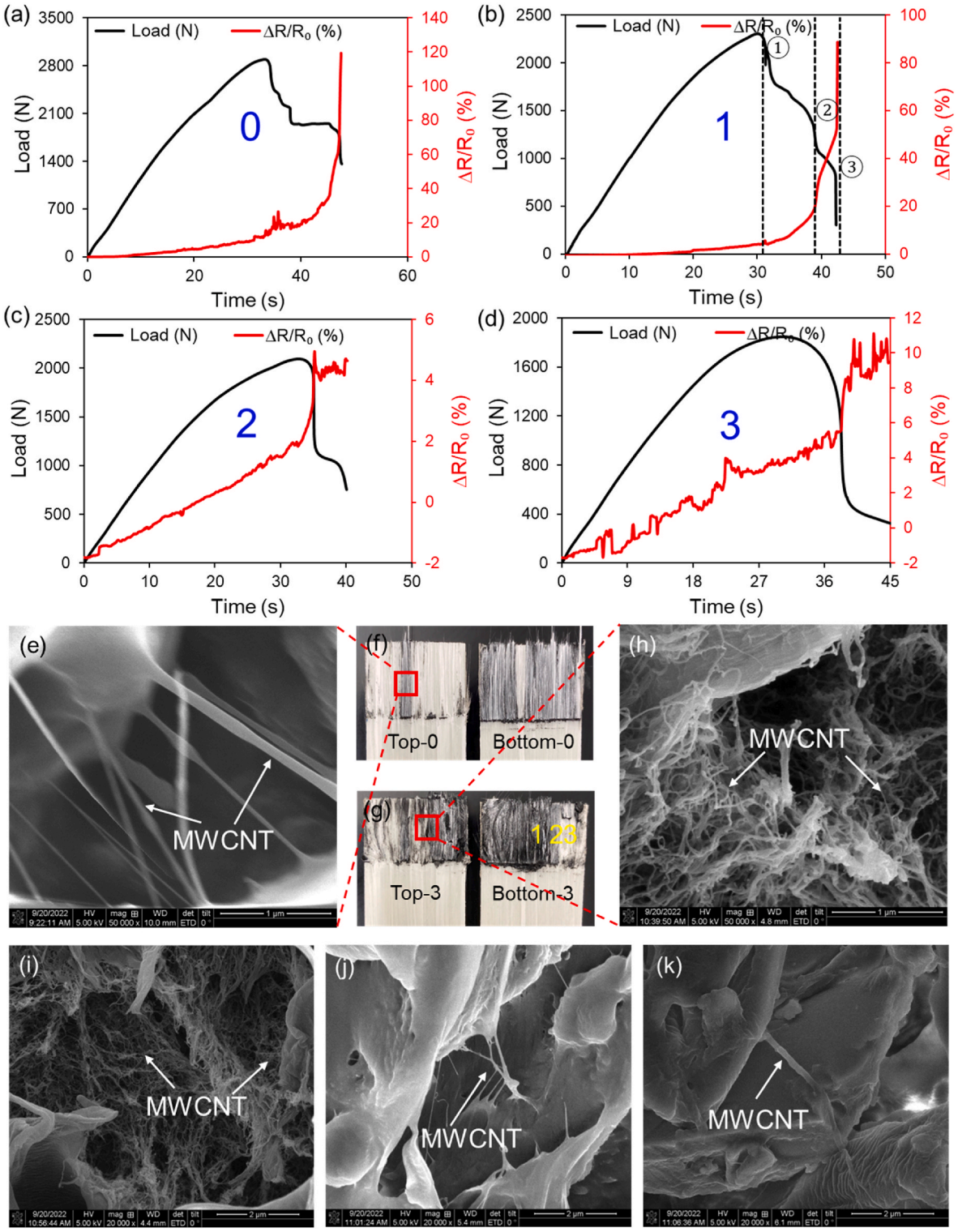

Fig. 6. Load and percentage change of electrical resistance curves during tensile testing for MWCNT/PP-GF/PP SLJs with different repair cycles: (a) initial (0), (b) first (1), (c) second (2), and (d) third (3); SEM images: (e) and (h) corresponding to the red frames in (f) and (g), respectively; (i), (j), and (k) corresponding to 1, 2, and 3 in (g), respectively. (For interpretation of the references to colour in this figure legend, the reader is referred to the Web version of this article.)

initiation occurring at step ①, indicating that some conductive pathways start breaking due to the increasing tensile loading. As damage accumulates, more and more conductive channels break, resulting in an exponential increase in resistance between step ② and step ③ until the repaired interface completely fractures, showing a large resistance increase. This behavior is in agreement with previous study on SLJs welded with MWCNT-based nanocomposite films subjected to tension [23]. Nanocomposite films still exhibit high sensitivity after the first repair cycle. However, for the second and third repair cycles, there is considerable noise in the electrical resistance profiles, especially in the latter (Fig. 6d). The unmolten nanocomposite film (Fig. 5c (iv)), the significant fracture patterns in Fig. 6g (1, 2, and 3), as well as less uniform distribution of conductive paths, confirmed in Fig. 6i–k, may be accountable for this noise. Nevertheless, a sudden increase in resistance can still be seen when the load drops in Fig. 6c and d. Resistance does not increase to infinity at the end of the tensile test for the second and third repaired SLJs, indicating that some connections still exist between MWCNTs. This is likely associated with a substantial amount of conductive networks created by the successive insertion of nanocomposite films at the interface (Fig. 6h), when compared to the initial joint shown in Fig. 6e.

Overall, every noticeable drop in load was always accompanied by a sharp jump in electrical resistance, showing that this MWCNT-based film has potential to monitor the initiation and propagation of damage occurring in the weld line of repaired TPC SLJs. However, its sensitivity seems to decrease with the repair cycles, which is less than 10% of $\Delta R/R_0$ (%) after the second and third repair cycle.

3.2. USW and RH repair without energy directors

3.2.1. Influence of process parameters on USW repair

To control the USW repair process, the downward vertical displacement of the sonotrode during the vibration phase (i.e., travel) was used. During regular welding, the travel value is related to how much material will be squeezed out at the interface and the quality of the welded joints [43,44]. Therefore, a range of travel values were studied for the repair process (20%, 40%, and 60% of the initial ED film thickness). The effect of travel on LSS of repaired SLJs is shown in Fig. 7a. On average, experimental results indicate that both low (20%) and high (60%) travel values lead to weaker joints, compared to 40% travel. On the one hand, if the travel value is low, then the ultrasonic vibration time is not long enough to uniformly melt the polymer at the interface to provide a strong bond and to remove air voids. As a result, failure mostly concentrates on one adherend (Fig. 7g) and voids are visible anywhere at the weld interface, whether at the edges or in the middle of the fracture surface, as shown in Fig. 7k and o, respectively, which can lead to poor bonding. On the other hand, a high travel value causes more outward squeeze flow of film with deformed fibers pushed to the sides, as well as transverse extrusion of GF/PP adherends (see the lap area in Fig. 7e), both responsible for the lower mechanical performance. In addition, there may be another factor contributing to the reduced LSS. In

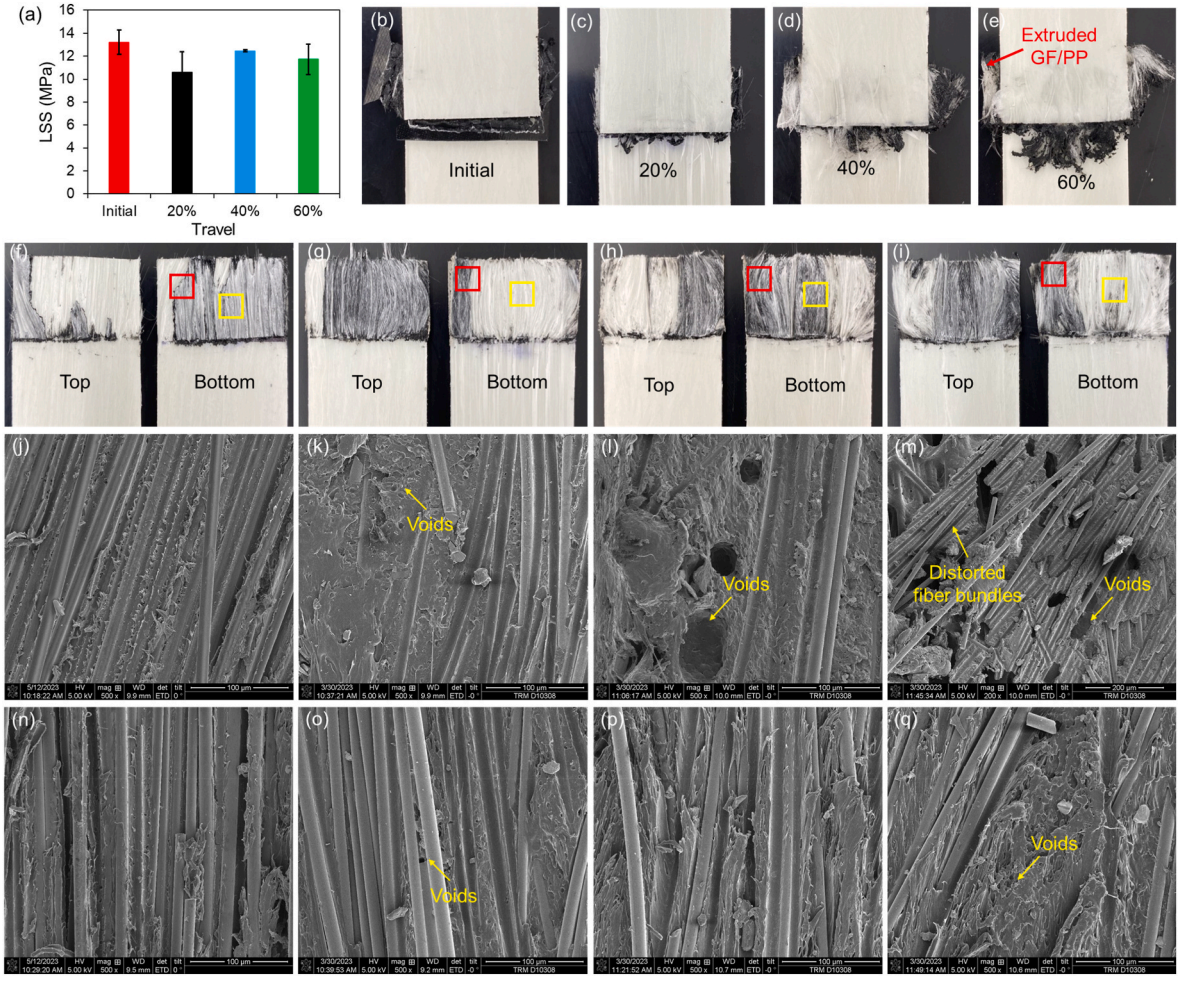

Fig. 7. USW repaired joints without EDs: (a) LSS at each travel value; (b–e) welded surfaces of reference weld, 20%, 40%, and 60% travel, respectively; (f–i) fracture surfaces of reference weld, 20%, 40%, and 60% travel, respectively; (j–m) SEM images corresponding to the red framed areas in (f–i), respectively; (n–q) SEM images corresponding to the yellow framed areas in (f–i), respectively. (For interpretation of the references to colour in this figure legend, the reader is referred to the Web version of this article.)

Fig. 7m, numerous large voids appear at the interface of the 60% travel specimen, different from the reference weld (Fig. 7j). Those voids were created during repair processing when most matrix was squeezed out of the weld line with the increasing displacement of the sonotrode up to 60% travel, resulting in a lack of resin to fill the gaps between fibers. Significant fiber distortion was found as the travel value increased. A travel value suitable for repair was found to be 40% according to the average LSS (94.3% of the initial joint) with low standard deviation. At this travel, air voids were generally removed, squeeze flow of film and adherends was limited, and fiber deformation was minimal. Morphological analysis revealed few voids, except at one edge of the fracture surface (Fig. 7l and p), and interlaminar failure in both adherends (Fig. 7h).

3.2.2. RH repair

In resistance heating, power can be supplied by current or voltage. For resistance heating repair, it was expected that due to the uneven fracture surfaces and potential gaps between nanocomposite film sections when both adherends are in contact (Fig. 8a), the heating performance could be negatively affected. Therefore, a series of preliminary tests were performed with various voltage levels, ranging from 20 to 40 V, as summarized in Table 1. It was found from this study that while delivering a voltage of 20 V, a long heating time was needed. Even after heating for 8 min, the temperature was generally steady between 80 °C and 90 °C, far below the melting point of PP due to the heat loss of the repair interface caused by the low heating rate at low power level. It was insufficient to soften the polymer matrix and initiate flow, resulting in poor or no bonding. However, when a high voltage of 40 V was applied, both GF/PP adherends melted through their thickness within 30 s and the temperature continued to increase rapidly after turning the power supply off, thereby causing GF/PP adherends to deteriorate. Most specimens under this voltage were tilted at an angle with respect to the other edge due to uneven melting of adherends at the interface. As a result, a large gap appeared at one end of the interface, shown in inset in Fig. 8b. After preliminary tests, and due to damaged adherends at 35 V, a constant voltage of 30 V was selected with a heating duration of 35–50 s, leading to even repair quality. The corresponding temperature profile as a function of heating time at a pressure of 0.2 MPa is shown in Fig. 8b. For this specimen, although the peak temperature of 156 °C is lower than the melting point of PP, no gaps were observed at the edges of the overlap. This lower temperature is due to the fact that only one thermocouple was positioned at the surface of the upper adherend, and it may not be representative of the temperature distribution for the entire repaired interface. In addition, during heating, the temperature at both edges of the joint is typically higher than other positions [28,29] because the edges are more exposed to the surrounding air, resulting in poor heat transfer, which in turn causes faster heating inside the heating element.

Table 1
Resistance heating parameters and performance.

Voltage	Heating duration (s)	Max temperature (°C)	Damage/repair condition
20 V	360–480	80–90	• Poor to no bonding
30 V	35–50	150–165	• Good repair quality • No gaps at the interface
35 V	25–40	160–200	• GF/PP adherends melted • Large amount of smoke • Slight tilt • No gaps at the interface
40 V	20–30	180–200	• GF/PP adherends melted • Large amount of smoke • Significant tilt • Gaps at the interface

In resistance heating repair, the electrical resistance of the heating element is another critical parameter, which directly affects the bonding effectiveness [38,45]. Therefore, the electrical resistance of the heating element was monitored, and a representative resistance profile is also shown in Fig. 8b. This plot illustrates that after an initial stabilization phase, the film's resistance increases with temperature. Nevertheless, the increase in electrical resistance was less than 7%, which is technically acceptable, as long as the resistance change does not exceed 10% [46] during the process.

3.2.3. Mechanical performance comparison between RH and USW repair

The LSS of repaired joints using RH and USW without an ED film at the interface is presented in Fig. 9a, including the reference specimens (before repair). LSS recovery was 94.3% and 85.1% for USW and RH repair, respectively. USW repaired specimens possess a small standard deviation (12.5 ± 0.1 MPa), while a larger standard deviation was obtained when using RH (10.6 ± 2.4 MPa). This significant standard deviation was expected since the heating time and maximum temperature eventually reached after stopping voltage supply varied from one specimen to another. Furthermore, scanning electron microscopy was used to observe the fracture surfaces of both samples at the center of the repaired region, as shown in Fig. 9b and c. Most fibers in the fracture surfaces of USW repaired joints were not bare. It is apparent in the magnified image that the fiber surfaces of USW repaired specimens were covered with thermoplastic matrix material, showing good fiber/matrix adhesion and thus, high bond strength. On the contrary, bare fiber surfaces for RH repaired specimens might have been a factor that

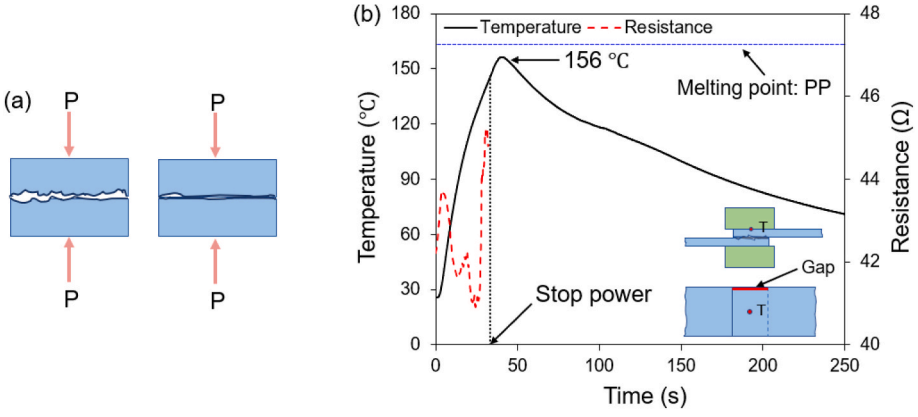

Fig. 8. (a) Cross-sections during RH repair illustrating potential gaps at the interface and (b) representative temperature and resistance profiles of specimens repaired under a pressure of 0.2 MPa and constant input voltage of 30 V. Inset shows position of thermocouple and overlap edge (red line) where gap was observed at the interface at a voltage of 40 V. (For interpretation of the references to colour in this figure legend, the reader is referred to the Web version of this article.)

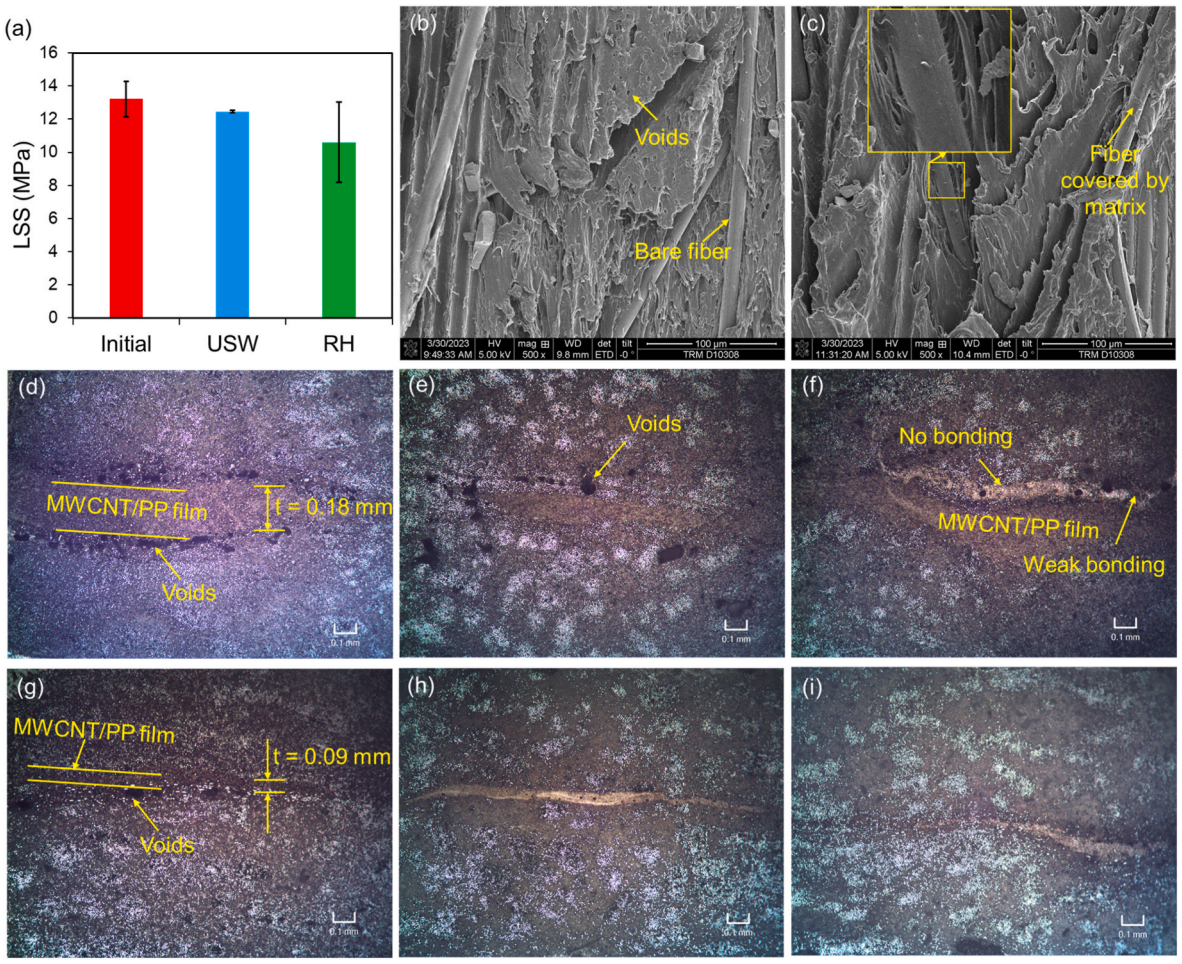

Fig. 9. RH and USW (40% travel) joints repaired without MWCNT/PP film insertion: (a) LSS values, where the red one relates to the reference specimens; (b, c) fracture surface SEM images of (b) RH and (c) USW repair at the center; (d–f) cross-sectional micrographs of RH repair at the (d) left edge, (e) center, and (f) right edge; and (g–i) cross-sectional micrographs of USW repair at the (g) left edge, (h) center, and (i) right edge. (For interpretation of the references to colour in this figure legend, the reader is referred to the Web version of this article.)

lowered their mechanical performance to a higher extent, compared to USW. On the other hand, matrix drawing was more extensive in USW repaired specimen (Fig. 9c) than for RH (lower matrix ductility) (Fig. 9b), corresponding to the higher strength for the former.

The bond quality of both repair techniques was further investigated by examining polished cross-sections under an optical microscope. Fig. 9d–f presents the left edge, center, and right edge of RH repaired joints, respectively. A high quantity of voids is observed, both at the edges and in the middle of the specimen. Additionally, the brighter band in Fig. 9f, between nanocomposite film and one of the GF/PP adherends, indicates that there is no actual bonding or weak bonding at the edge of the repaired joint, causing epoxy resin to flow in. This may be a result from the non-uniform temperature distribution during heating (based on non-uniform contact depicted in Fig. 8a) or a different pressure distribution between the left and right edges due to the tilt of the spring clamps. USW processing seems to result in a more uniform repair quality, as shown in Fig. 9g–i. The bond between nanocomposite film and both adherends looks complete and few voids are present (only at one edge of the weld interface presented in Fig. 9g).

Overall, both repair methods demonstrated strength recovery above 85%, with more consistent quality for USW repair. However, even though the mechanical performance of USW repaired joints was better than RH repair, more squeezed out nanocomposite film at the weld line and a thinner thickness (Fig. 9g) may lessen the capabilities of strain sensing and damage monitoring of the nanocomposite films.

4. Conclusions

In this study, ultrasonically welded single-lap GF/PP joints were repaired using ultrasonic welding and resistance heating methods. Cyclic repair with the successive use of energy director films and direct, one-step repair after fracture were carried out. The repair effectiveness of the two techniques was analyzed using tensile testing, optical microscopy, scanning electron microscopy, and electrical resistance measurements. The main conclusions drawn from this experimental investigation are the following:

- Pure PP films were used to repair welded GF/PP joints for three successive cycles, with a lap shear strength recovery of 94.5%, 89.4%, and 86.7%. MWCNT/PP films partially restored the strength to a lesser extent, 81.3%, 73.6%, and 63.8%, due to their brittleness, thicker weld line, and more significant fiber deformation.
- The MWCNT/PP nanocomposite films investigated in this study hold promise for examining the initiation and propagation of damage within repaired single lap thermoplastic composite joints, even after three repair cycles.
- The downward displacement of the sonotrode during the USW process (or “travel”) has an important effect on the strength of repaired joints. Voids were visible in the entire fracture surfaces under low travel repair (LSS of 10.6 ± 1.8 MPa for 20% travel), while high travel (LSS of 11.7 ± 1.3 MPa for 60% travel) squeezed more film out and caused transverse extrusion of GF/PP adherends at the interface.

An optimum travel value of 40% (LSS of 12.5 ± 0.1 MPa) was determined.

- Resistance heating assisted repair yielded a LSS of 10.6 ± 2.4 MPa with a strength recovery of 85.1%, compared to ultrasonically repaired joints with a LSS of 12.5 ± 0.1 MPa (94.3%). For resistance heating repair, absence of resin flow during heating led to unbonded area at the edge and several voids caused by non-uniform temperature distribution at the weld interface. On the other hand, for ultrasonic welding repair, scanning electron microscopy and optical microscopy showed that repair quality was uniform over the welded interface and voids were only observed at the edge of the joints.

Overall, the strength recovery performance of USW and RH repair methods was between 63.8% and 94.5%, demonstrating their potential for TPC joints. However, nanocomposite films typically lower mechanical properties of thermoplastic composite joints, compared to pure PP films. Future work will thus focus on investigating methods to close the gap of decreased lap shear strength, for example, incorporating plasticizers into nanocomposite films to reduce their brittleness and inserting nanocomposite strips between pure PP films while maintaining electrical conductivity.

Applicability of the proposed methods on real-life structures should also be the topic of future work. While repair of monolithic and/or thin structures and components that can be removed (e.g., doors) would be feasible for both USW and resistance heating repair, in-field repair presents unique challenges. Welding techniques should employ standard and simple equipment, but the area to be repaired also requires support to apply sufficient pressure during fusion bonding and to prevent deformation during the process. Based on the setups used in this study, resistance heating is simpler than USW for potential in-field repair, but further research should be conducted to assess applicability of both methods.

CRediT author statement

Wencai Li: Conceptualization, Methodology, Formal Analysis, Investigation, Visualization, Writing- Original draft. Genevieve Palardy: Funding acquisition, Supervision, Writing- Reviewing and Editing.

Declaration of competing interest

The authors declare that they have no known competing financial interests or personal relationships that could have appeared to influence the work reported in this paper.

Data availability

Data will be made available on request.

Acknowledgements

This work was supported by the National Science Foundation CAREER award (CMMI, Advanced Manufacturing, Award #2045955); the Louisiana Board of Regents under the Research Competitiveness Subprogram (contract number LEQSF (2018–2023)-RD-A-05); and the LSU Graduate School Economic Development Assistantship.

References

[1] Sahoo CK, Bhatia GS, Arockiarajan A. Effect of patch-parent stacking sequence and patch stiffness on the tensile behaviour of the patch repaired carbon-glass hybrid composite. Thin-Walled Struct 2022;179:109551.
[2] Rito RL, Crocombe AD, Ogin SL. Health monitoring of composite patch repairs using CFBG sensors: experimental study and numerical modelling. Composites Part A Appl Sci Manuf 2017;100:255–68.
[3] Cao D, Hu H, Wang Y, Li S. Experimental and numerical studies on influence of impact damage and simple bolt repair on compressive failure of composite laminates. Compos Struct 2021;275:114491.
[4] Barroeta Robles J, Dubé M, Hubert P, Yousefpour A. Repair of thermoplastic composites: an overview. Adv Manuf Polym Compos Sci 2022;8(2):68–96.
[5] Hall ZEC, Liu J, Brooks RA, Liu H, Crocker JWM, Joesbury AM, et al. The effectiveness of patch repairs to restore the impact properties of carbon-fibre reinforced-plastic composites. Eng Fract Mech 2022;270:108570.
[6] Ji X, Zhou W, Sun H, Liu J, Ma L-h. Damage evolution behavior of bi-adhesive repaired composites under bending load by acoustic emission and micro-CT. Compos Struct 2022;279:114742.
[7] Zhou W, Ji X-l, Yang S, Liu J, Ma L-h. Review on the performance improvements and non-destructive testing of patches repaired composites. Compos Struct 2021;263:113659.
[8] Bhatia GS, Arockiarajan A. Fatigue studies on patch repaired carbon/epoxy woven composites. Compos B Eng 2019;175:107121.
[9] Li G, Ji G, Zhenyu O. Adhesively bonded healable composite joint. Int J Adhesion Adhes 2012;35:59–67.
[10] Loh TW, Ladani RB, Orifici A, Kandare E. Ultra-tough and in-situ repairable carbon/epoxy composite with EMAA. Composites Part A Appl Sci Manuf 2021;143:106206.
[11] Loh TW, Ladani RB, Ravindran A, Das R, Kandare E, Mouritz AP. Z-Pinned composites with combined delamination toughness and delamination Self-Repair properties. Composites Part A Appl Sci Manuf 2021;149:106566.
[12] Brito C BG, Teuwen J, Dransfeld CA, Villegas I F. The effects of misaligned adherends on static ultrasonic welding of thermoplastic composites. Composites Part A Appl Sci Manuf 2022;155.
[13] Bourda P, Mbacké MA, Rozycki P. Experimental investigation of the loading speed effects on the performances of ultrasonically welded PA66/glass fabric composites. Compos B Eng 2023:253.
[14] Jongbloed B, Teuwen J, Benedictus R, Villegas IF. On differences and similarities between static and continuous ultrasonic welding of thermoplastic composites. Compos B Eng 2020;203:108466.
[15] Jongbloed B, Vinod R, Teuwen J, Benedictus R, Villegas IF. Improving the quality of continuous ultrasonically welded thermoplastic composite joints by adding a consolidator to the welding setup. Composites Part A Appl Sci Manuf 2022;155:106808.
[16] Wang Y, Rao Z, Liao S, Wang F. Ultrasonic welding of fiber reinforced thermoplastic composites: current understanding and challenges. Composites Part A Appl Sci Manuf 2021:149.
[17] Zhao Q, Gao Z, Wang H, Wu H, Chen X, Qu Z, et al. On accurate characterization of interfacial morphology and damage evolution of thermoplastic composite welded joints: a microscale study via in-situ micro-CT. Compos Sci Technol 2023:236.
[18] Zhao T, Zhao Q, Wu W, Xi L, Li Y, Wan Z, et al. Enhancing weld attributes in ultrasonic spot welding of carbon fibre-reinforced thermoplastic composites: effect of sonotrode configurations and process control. Compos B Eng 2021:211.
[19] Lee TH, Fan H-T, Li Y, Shriver D, Arinez J, Xiao G, et al. Enhanced performance of ultrasonic welding of short carbon fiber polymer composites through control of morphological parameters. J Manuf Sci Eng 2020;142(1).
[20] Li Y, Yu B, Wang B, Lee TH, Banu M. Online quality inspection of ultrasonic composite welding by combining artificial intelligence technologies with welding process signatures. Mater Des 2020;194:108912.
[21] Tutunjian S, Dannemann M, Fischer F, Eroğlu O, Modler N. A control method for the ultrasonic spot welding of fiber-reinforced thermoplastic laminates through the weld-power time derivative. Journal of Manufacturing and Materials Processing 2018;3(1).
[22] Yang Y, Li Y, Liu Z, Li Y, Ao S, Luo Z. Ultrasonic welding of short carbon fiber reinforced PEEK with spherical surface anvils. Compos B Eng 2022:231.
[23] Li W, Frederick H, Palardy G. Multifunctional films for thermoplastic composite joints: ultrasonic welding and damage detection under tension loading. Composites Part A Appl Sci Manuf 2021;141:106221.
[24] Li W, Palardy G. Electro-mechanical response of ultrasonically welded thermoplastic composite interfaces under static and cyclic flexural loads using nanocomposites. ACS Applied Polymer Materials 2022;4(7):5209–23.
[25] Li W, Palardy G. Damage monitoring methods for fiber-reinforced polymer joints: a review. Compos Struct 2022;299:116043.
[26] Frederick H, Li W, Palardy G. Disassembly study of ultrasonically welded thermoplastic composite joints via resistance heating. Materials 2021;14(10):2521.
[27] Li W, Palardy G. Tensile behavior of repaired thermoplastic composite joints through ultrasonic welding. Seattle: Society for the Advancement of Material and Process Engineering; 2023. WA.
[28] Ageorges C, Ye L, Hou M. Experimental investigation of the resistance welding for thermoplasttic-matrix composites. Part I heating element and heat transfer. Compos Sci Technol 2000;60:1027–39.
[29] Hou M, Friedrich K. Resistance welding of continuous carbon fibre polypropylene compoistes. Plast, Rubber Compos Process Appl 1992;18(4):205–13.
[30] Hou M, Friedrich K. Resistance welding of continuous glass fibre-reinforced polypropylene compoistes. Compos Manuf 1992;3(3):153–63.
[31] Ageorges C, Ye L, Hou M. Experimental investigation of the resistance welding of thermoplastic-matrix composites. Part II optimum processing window. Compos Sci Technol 2000;60:1191–202.
[32] Xiong X, Wang D, Wei J, Zhao P, Ren R, Dong J, et al. Resistance welding technology of fiber reinforced polymer composites: a review. J Adhes Sci Technol 2021;35(15):1593–619.
[33] Dubé M, Hubert P, Yousefpour A, Denault J. Resistance welding of thermoplastic composites skin/stringer joints. Composites Part A Appl Sci Manuf 2007;38(12):2541–52.

[34] Barbosa LCM, de Souza SDB, Botelho EC, Cândido GM, Rezende MC. Fractographic evaluation of welded joints of PPS/glass fiber thermoplastic composites. Eng Fail Anal 2019;102:60–8.
[35] Brassard D, Dubé M, Tavares JR. Modelling resistance welding of thermoplastic composites with a nanocomposite heating element. J Compos Mater 2020;0(0):1–15.
[36] Brassard D, Dubé M, Tavares JR. Resistance welding of thermoplastic composites with a nanocomposite heating element. Compos B Eng 2019;165:779–84.
[37] Bonmatin M, Chabert F, Bernhart G, Cutard T, Djilali T. Ultrasonic welding of CF/PEEK composites: influence of welding parameters on interfacial temperature profiles and mechanical properties. Composites Part A Appl Sci Manuf 2022:162.
[38] Stavrov D, Bersee HEN. Resistance welding of thermoplastic composites-an overview. Composites Part A Appl Sci Manuf 2005;36(1):39–54.
[39] Verma P, Ubaid J, Varadarajan KM, Wardle BL, Kumar S. Synthesis and characterization of carbon nanotube-doped thermoplastic nanocomposites for the additive manufacturing of self-sensing piezoresistive materials. ACS Appl Mater Interfaces 2022;14(6):8361–72.
[40] Zetina-Hernández O, Duarte-Aranda S, May-Pat A, Canché-Escamilla G, Uribe-Calderon J, Gonzalez-Chi PI, et al. Coupled electro-mechanical properties of multiwall carbon nanotube/polypropylene composites for strain sensing applications. J Mater Sci 2013;48(21):7587–93.
[41] Ma Y, Yang Y, Sugahara T, Hamada H. A study on the failure behavior and mechanical properties of unidirectional fiber reinforced thermosetting and thermoplastic composites. Compos B Eng 2016;99:162–72.
[42] Mishnaevsky L, Brøndsted P. Micromechanical modeling of damage and fracture of unidirectional fiber reinforced composites: a review. Comput Mater Sci 2009;44(4):1351–9.
[43] Villegas IF. Strength development versus process data in ultrasonic welding of thermoplastic composites with flat energy directors and its application to the definition of optimum processing parameters. Composites Part A Appl Sci Manuf 2014;65:27–37.
[44] Tsiangou E, Kupski J, Teixeira de Freitas S, Benedictus R, Villegas IF. On the sensitivity of ultrasonic welding of epoxy- to polyetheretherketone (PEEK)-based composites to the heating time during the welding process. Composites Part A Appl Sci Manuf 2021;144:106334.
[45] Du B, Chen L, Liu H, He Q, Qin W, Li W. Resistance welding of glass fiber reinforced thermoplastic composite: experimental investigation and process parameter optimization. Chin J Aeronaut 2020;33(12):3469–78.
[46] Ageorges C, Ye L. Fusion bonding of polymer composites. Springer Science & Business Media; 2012.